Thermoelectric properties of inversion symmetry broken Weyl semimetal–Weyl superconductor hybrid junctions

Ruchi Saxena [1,2,*] Nirnoy Basak,[3,4,*] Pritam Chatterjee [5,4,*] Sumathi Rao [6,3,†] and Arijit Saha [5,4,‡]

[1]*Advanced Technology Institute and Department of Physics, University of Surrey, Guildford GU2 7XH, United Kingdom*
[2]*National Physical Laboratory, Hampton Road, Teddington TW11 0LW, United Kingdom*
[3]*Harish-Chandra Research Institute, Chhatnag Road, Jhunsi, Allahabad, Uttar Pradesh 211 019, India*
[4]*Homi Bhabha National Institute, Training School Complex, Anushakti Nagar, Mumbai 400094, India*
[5]*Institute of Physics, Sachivalaya Marg, Bhubaneswar, Orissa 751005, India*
[6]*International Centre for Theoretical Sciences (ICTS-TIFR), Shivakote, Hesaraghatta Hobli, Bangalore 560089, India*

We theoretically investigate the thermoelectric properties (electronic contribution) of a hybrid structure comprising an inversion symmetry broken Weyl semimetal (WSM) and intrinsic Weyl superconductor (WSC) with *s*-wave pairing, employing the Blonder-Tinkham-Klapwijk formulation for noninteracting electrons. Our study unfolds interesting features for various relevant physical quantities such as thermal conductance, the thermoelectric coefficient, and the corresponding figure of merit. We also explore the effects of an interfacial insulating (I) barrier (WSM-I-WSC setup) on the thermoelectric response in the thin barrier limit. Further, we compute the ratio of the thermal to the electrical conductance in different temperature regimes and find that the Wiedemann-Franz law is violated for small temperatures (below critical temperature T_c) near the Weyl points while it saturates to the Lorentz number, away from the Weyl points, at all temperatures irrespective of the barrier strength. We compare and contrast this behavior with other Dirac material heterostructures and provide a detailed analysis of the thermal transport. Our study can facilitate the fabrication of mesoscopic thermoelectric devices based on WSMs.

I. INTRODUCTION

In recent times, Weyl semimetals (WSMs) have been subject to intense theoretical and experimental investigations as they are explicit material realizations of hitherto high-energy phenomena, such as the Adler-Bell-Jackiw anomaly [1,2] and the chiral magnetic effect [3]. In terms of their band structure, WSMs exhibit linearly dispersing excitations from nondegenerate band touching points called Weyl nodes accompanying unusual surface projections known as Fermi arcs [4]. Weyl nodes always appear in pairs of opposite chirality and behave as oppositely charged monopoles of Berry flux because the electronic states around the band touching points have nonzero Berry curvature. This gives rise to nontrivial topology in momentum space due to which WSMs exhibit several interesting physical effects, such as the quantum anomalous Hall effect, the chiral magnetic effect, negative magnetoresistance, etc. [4–8]. Intense theoretical and experimental research work has been carried out in both time-reversal and inversion symmetry broken WSMs [4,5,9].

In principle, the WSM phase can be realized by breaking either the time reversal (TR) or the inversion symmetry (IS) [4,7,10,11]. Breaking of the TR symmetry requires a large external magnetic field, which limits the use and application of these materials. However, recently, a WSM state was confirmed in transition-metal mono-phosphide or mono-arsenide *MX* materials (*M*=Nb and Ta; *X*=P and As) with naturally broken IS due to crystal structure asymmetry [5,12–16]. In these materials, the Weyl nodes and surface Fermi arcs are detected by using angle-resolved photoemission spectroscopy (ARPES).

Over the past years, superconducting hybrid structures have attracted a great deal of attention due to the dramatic boosts of thermoelectric effects in them [17–24]. In order to investigate the thermoelectric properties of a material or hybrid junction, it is customary to compute the thermal conductance or thermal current generated by the applied temperature gradient. From the application point of view, it is more desirable to investigate the Seebeck coefficient, known as thermopower. A better way to examine the efficiency of a system as a thermoelectric is to study the thermopower as well as a dimensionless parameter called the figure of merit (zT) [25]. Improving this thermoelectric zT along with enhanced Seebeck coefficient is one of the main challenges in materials science [26], as well as mesoscopic hybrid junctions [27]. Along this direction, heat transport has also been investigated in superconducting heterostructures of two-dimensional Dirac systems [28–33].

Although electronic properties of WSMs (both in bulk and heterojunctions) have been extensively studied in recent times [34–39], far less is known about its thermoelectric properties

---

*These authors contributed equally to this work.
†sumathi.rao@ictis.res.in
‡arijit@iopb.res.in

as far as hybrid junctions are concerned. There have been earlier studies including disorder and interactions both near the Weyl point and with doping away from the Weyl point [12, 40–42]. However, these works only investigate thermoelectric properties in the bulk material. Heterojunctions, which form the foundation of applications in electronics and spintronics, have not yet been explored in the context of their thermal properties involving WSMs and superconductivity. Motivated by this fact, in this article we focus on this gap and explicitly study the thermal properties of a heterojunction consisting of an inversion symmetry broken WSM (normal region) on one side and a bulk Weyl superconductor (WSC) [43–45] on the other side, thus tailoring a WSM-WSC junction. In particular, we obtain the electronic contribution to the thermal conductivity, the Seebeck coefficient and the figure of merit (that is, the ratio of the Seebeck coefficient and the thermal conductivity) for this setup. Note that a similar analysis cannot be carried out for a TR broken WSM-WSC junction, as Andreev reflection is fully suppressed there in the absence of a spin active interface, due to chirality blockade [46].

The remainder of this paper is organized as follows. In Sec. II we describe the model Hamiltonian of IS broken WSM and the scattering matrix approach to analyze our setup. Section III is devoted to the analytical formulas for computing various physical quantities that are required to assess the thermoelectric properties of the system. We discuss the numerical results of the WSM-WSC junction in Sec. IV. Finally, we summarize our findings and discuss some possible outlooks in Sec. V.

II. MODEL AND METHOD

In this section we describe the model Hamiltonian of our setup and discuss the scattering matrix approach to analyze the junction problem.

A. Model Hamiltonian

To begin with, we consider an inversion asymmetric WSM described by the Hamiltonian [47], $\mathcal{H} = \sum_{\mathbf{k}} \psi_{\mathbf{k}}^\dagger H(\mathbf{k}) \psi_{\mathbf{k}}$, with

$$H(\mathbf{k}) = k_x \sigma_x s_z + k_y \sigma_y s_0 + (k_0^2 - |\mathbf{k}|^2) \sigma_z s_0$$
$$+ \beta \sigma_y s_y - \alpha k_y \sigma_x s_y, \quad (1)$$

where $\mathbf{k} = (k_x, k_y, k_z)$, $\psi_{\mathbf{k}}^\dagger = (c_{A,\uparrow,\mathbf{k}}^\dagger, c_{A,\downarrow,\mathbf{k}}^\dagger, c_{B,\uparrow,\mathbf{k}}^\dagger, c_{B,\downarrow,\mathbf{k}}^\dagger)$, and $c_{\sigma,s,\mathbf{k}}^\dagger$ are creation operators with $\vec{\sigma}$ and $\vec{s}$ Pauli matrices for the orbital (A,B) and spin degrees of freedom ($\uparrow, \downarrow$) in the z direction, respectively. Here, $k_0, \alpha,$ and β denote real model parameters. For $k_0 > \beta$, the model exhibits four Weyl nodes at Q_γ as shown in Fig. 1(a), where we label $Q_{\gamma=1,2,3,4}$ as $(\beta, 0, \sqrt{k_0^2 - \beta^2})$, $(-\beta, 0, -\sqrt{k_0^2 - \beta^2})$, $(\beta, 0, -\sqrt{k_0^2 - \beta^2})$, and $(-\beta, 0, \sqrt{k_0^2 - \beta^2})$, respectively. We schematically depict the positions of the four Weyl nodes in Fig. 1(b), choosing the $k_x - k_z$ plane intersecting at $k_y = 0$.

Using the transformation $c_{s,\mathbf{k}}^{(\sigma)} = (c_{\sigma,\uparrow,\mathbf{k}} \pm c_{\sigma,\downarrow,\mathbf{k}})/\sqrt{2}$ [47], where $\mathbf{s} = (\uparrow, \downarrow)$ denotes the spin in the x direction in this new basis, we can write the low-energy Hamiltonian as the sum of four 2×2 Hamiltonians near the four Weyl nodes as $\mathcal{H}_W = \sum_{\gamma=1}^{4} \sum_{\mathbf{k}}' \Psi_{\gamma,\mathbf{k}}^\dagger H_\gamma \Psi_{\gamma,\mathbf{k}}$, where $\Psi_{1,\mathbf{k}}^\dagger = \Psi_{3,\mathbf{k}}^\dagger = (c_{\uparrow,\mathbf{k}}^{B\dagger}, c_{\downarrow,\mathbf{k}}^{A\dagger})$ and $\Psi_{2,\mathbf{k}}^\dagger = \Psi_{4,\mathbf{k}}^\dagger = (c_{\uparrow,\mathbf{k}}^{A\dagger}, c_{\downarrow,\mathbf{k}}^{B\dagger})$
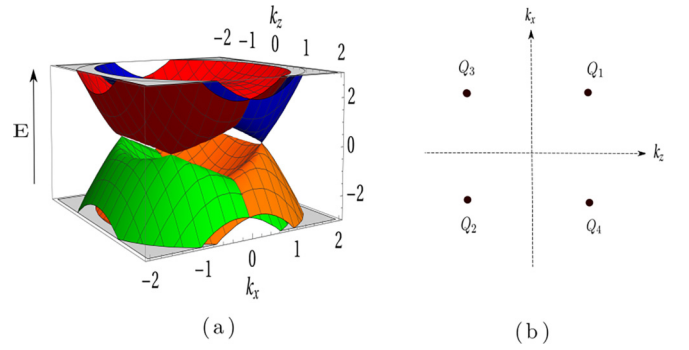
FIG. 1. (a) Band structure of IS broken WSM, modeled by the low-energy effective Hamiltonian [Eq. (1)], is shown at $k_y = 0$ for fixed values of $\beta = 1$ and $\alpha = \sqrt{2}$. (b) The positions of the Weyl nodes ($Q_{\gamma=1,2,3,4}$) are shown schematically in the $k_x - k_z$ plane choosing $k_y = 0$.

[47]. Here $\sum_{\mathbf{k}}'$ indicates the fact that crystal momenta k_x, k_y, k_z are now restricted close to the Weyl points. The Hamiltonian H_γ can be written as [47]

$$H_{1,2} = (k_x \mp \beta) s_x + k_y s_y + (k_z \mp \sqrt{k_0^2 - \beta^2}) s_z,$$

$$H_{3,4} = (k_x \mp \beta) s_x + k_y s_y - (k_z \pm \sqrt{k_0^2 - \beta^2}) s_z. \quad (2)$$

Here k_y and k_z are rescaled by $1/\alpha$ and $1/2\sqrt{k_0^2 - \beta^2}$. The Weyl points Q_1 and Q_2 (Q_3 and Q_4) carry the positive (negative) chirality and form two time-reversed pairs.

We assume that the system remains metallic with an approximately linear dispersion, even in the presence of disorder. This remains a good approximation as long as the Fermi energy is larger than the disorder-induced gap in the system [42]. Beyond that, we consider intraorbital s-wave superconducting pairing which couples Weyl nodes of the same chirality. This is because at low energy, the interorbital pairing is known to be suppressed [37]. Consequently, we can consider two decoupled superconducting Hamiltonians with opposite chirality as [37]

$$H_S^+ = \sum_{\mathbf{k}}' (\Delta c_{1,\uparrow,\mathbf{k}}^\dagger c_{2,\downarrow,-\mathbf{k}}^\dagger + 1 \leftrightarrow 2) + \text{H.c.}, \quad (3)$$

$$H_S^- = \sum_{\mathbf{k}}' (\Delta c_{3,\uparrow,\mathbf{k}}^\dagger c_{4,\downarrow,-\mathbf{k}}^\dagger + 3 \leftrightarrow 4) + \text{H.c.}, \quad (4)$$

where $c_{1,\uparrow,\mathbf{k}}^\dagger$ and $c_{2,\downarrow,\mathbf{k}}^\dagger$ in Eq. (3) [or $c_{3,\uparrow,\mathbf{k}}^\dagger$ and $c_{4,\downarrow,\mathbf{k}}^\dagger$ in Eq. (4)] are creation operators at Weyl points 1 and 2 (or 3 and 4), respectively. The pairing potential Δ couples electrons and holes only between the time-reversed pair of Weyl nodes, i.e., Q_1 to Q_2 and Q_3 to Q_4. Here $\uparrow$ and $\downarrow$ represent the spin in x direction.

We analyze the heterostructure comprising a WSM and a bulk WSC with s-wave pairing, considering the above-mentioned model Hamiltonians. Our WSM-WSC setup is illustrated in Fig. 2. The thin violet region at the interface (see Fig. 2) indicates an insulating barrier with width d and height V_0. We incorporate this to investigate thin barrier effects on thermal transport through the junction.

Considering quasi-one-dimensional transport along the z direction, we can write the Bogoliubov–de Gennes (BdG) Hamiltonian for the positive chirality sector as an 8×8
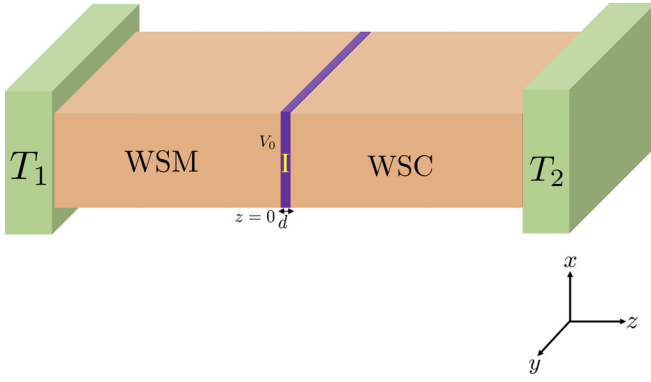
FIG. 2. Schematic diagram of our setup in which the WSM part is treated as the normal (N) region while the other side is a WSC with *s*-wave pairing (superconducting region S), thus forming a WSM-WSC heterostructure (orange). The green regions indicate the left and right reservoirs maintained at thermal equilibrium with temperatures T_1 and T_2, respectively, and at a finite voltage bias eV. A thin violet region symbolizes the insulating (I) barrier of width d and height V_0 sandwiched between the normal and superconducting regions.

Hamiltonian,

$$\mathcal{H}_+ = \begin{pmatrix} h^1_{\text{BdG}} & \emptyset \\ \emptyset & h^2_{\text{BdG}} \end{pmatrix},$$ (5)

where $\emptyset$ is a 4×4 null matrix, and each of the diagonal Hamiltonian can be written as

$$h^1_{\text{BdG}} = \begin{pmatrix} \text{Weyl node 1} & & \Delta & 0 \\ \text{(electron space)} & & 0 & \Delta \\ \Delta^* & 0 & \text{Weyl node 2} & \\ 0 & \Delta^* & \text{(hole space)} & \end{pmatrix}$$

and

$$h^2_{\text{BdG}} = \begin{pmatrix} \text{Weyl node 2} & & \Delta & 0 \\ \text{(electron space)} & & 0 & \Delta \\ \Delta^* & 0 & \text{Weyl node 1} & \\ 0 & \Delta^* & \text{(hole space)} & \end{pmatrix}.$$ (6)

Here, h^1_{BdG} and h^2_{BdG} effectively represent the same BdG Hamiltonian. We focus only on h^1_{BdG} for the purpose of this paper. Using the Nambu basis in real space $(\Psi_{1,\uparrow}, \Psi_{1,\downarrow}, \Psi^\dagger_{2,\downarrow}, -\Psi^\dagger_{2,\uparrow})$, we can write h^1_{BdG} as

$$h^1_{\text{BdG}} = v_z[-i\partial_r \cdot \mathbf{s} - \mu(z)\, s_0] + \Delta(z)\, v_x\, s_0 \,.$$ (7)

Here, Pauli matrices v and $\mathbf{s}$ act on Weyl points and spin, respectively. Considering the electronic transport along the z direction, we define chemical potential μ and superconducting pairing potential $\Delta(z)$ for the geometry shown in Fig. 2 as

$$\mu(z) = \mu_N\, \Theta(-z) + \mu_S\, \Theta(z) \,,$$
$$\Delta(z) = \Delta(T)\, e^{i\alpha}\, \Theta(z) \,.$$ (8)

The temperature-dependent superconducting gap is $\Delta(T) = \Delta_0 \tanh(1.74\sqrt{T_c/T - 1})$. $\Theta(z)$ is the Heaviside step function, α is the phase of the superconducting order parameter, which is fixed at zero for simplicity, and T_c is

the critical temperature of the superconductor. Here, μ_N and μ_S are the chemical potentials on WSM and WSC sides, respectively. Furthermore, we introduce a unitary transformation in order to transfer the k_0 and β dependence of the Hamiltonian to the wave function [37].

Similarly, one can write the BdG Hamiltonian for the negative chirality sector (H_-) by replacing ∂_z by $-\partial_z$. We focus only on the positive chirality sector in this work, and it is straightforward to extend the thermal transport analysis for the negative chirality Weyl fermions.

The mean-field theory of superconductivity demands that $\mu_S \gg \Delta_0$, or equivalently, that the superconducting coherence length ξ is much larger than the Fermi wavelength in the superconducting region [48]. Note that we fix $\mu_S = 100\Delta_0$ to satisfy this requirement throughout our analysis.

To understand the nature of normal and Andreev reflection (AR) at the interface between WSM and WSC, it is necessary to analyze the spin texture around the Weyl nodes for both electrons and holes. For this we employ the low-energy Hamiltonians [Eq. (2)] to find the expectation values of spin vector for the lower conduction band around each Weyl point and show them in Fig. 3. It is evident from Fig. 3(a) that the conduction electron incident from Weyl point Q_1 is reflected as a normal electron from the opposite Fermi surface at Q_3 to preserve the spin quantum number. The hole due to retro-AR comes from the time-reversed partner, which is at $Q'_1 = -Q_1$ and carries opposite texture compared to the incoming electron. This is schematically shown in Fig. 3(b). Specular AR takes place from the valence band of the hole, and this is depicted in Fig. 3(c).

B. Scattering matrix approach

Due to the superconducting pairing between the time-reversed pairs of Weyl nodes with the same chirality [37], we can separately compute contributions arising from the positive and negative chirality Weyl nodes. Considering the positive chirality Weyl nodes in our study, we investigate the thermal transport employing the scattering matrix approach [23,49,50] for the noninteracting electrons in the WSM-WSC setup (see Fig. 2). Let us consider the electronic transport along the perpendicular direction to the interface between the normal and superconducting part of the WSM, which means that the momentum parallel to the interface $k_{||} (= k_x, k_y)$ is conserved. We consider the excitation energy $E > 0$, such that the incoming electron is above the Fermi level at energy $\mu_N + E$, while the Andreev-reflected hole is at energy $\mu_N - E$.

Using BdG Hamiltonian for the WSM-WSC junction, the wave functions in the normal side (WSM) for a given excitation energy E can be written as

$$\psi_{\overrightarrow{e}}(z) = (\cos\varphi_e, e^{i\theta_k}\sin\varphi_e, 0, 0)^T e^{ik_e z} \,,$$
$$\psi_{\overleftarrow{e}}(z) = (e^{-i\theta_k}\sin\varphi_e, \cos\varphi_e, 0, 0)^T e^{-ik_e z} \,,$$
$$\psi_{\overrightarrow{h}}(z) = (0, 0, -e^{-i\theta_k}\sin\varphi_h, \cos\varphi_h)^T e^{ik_h z} \,,$$
$$\psi_{\overleftarrow{h}}(z) = (0, 0, \cos\varphi_h, -e^{i\theta_k}\sin\varphi_h)^T e^{-ik_h z} \,,$$ (9)

where $k_{(e,h)} = \sqrt{(E \pm \mu_N)^2 - k_{||}^2}$ are the momenta of the electron and hole, respectively, $\varphi_{(e,h)} = \tan^{-1}(k_{||}/k_{(e,h)})/2$ are the incident angles of the incoming electron and hole, respectively, and $\theta_k = \tan^{-1}(k_y/k_x)$.
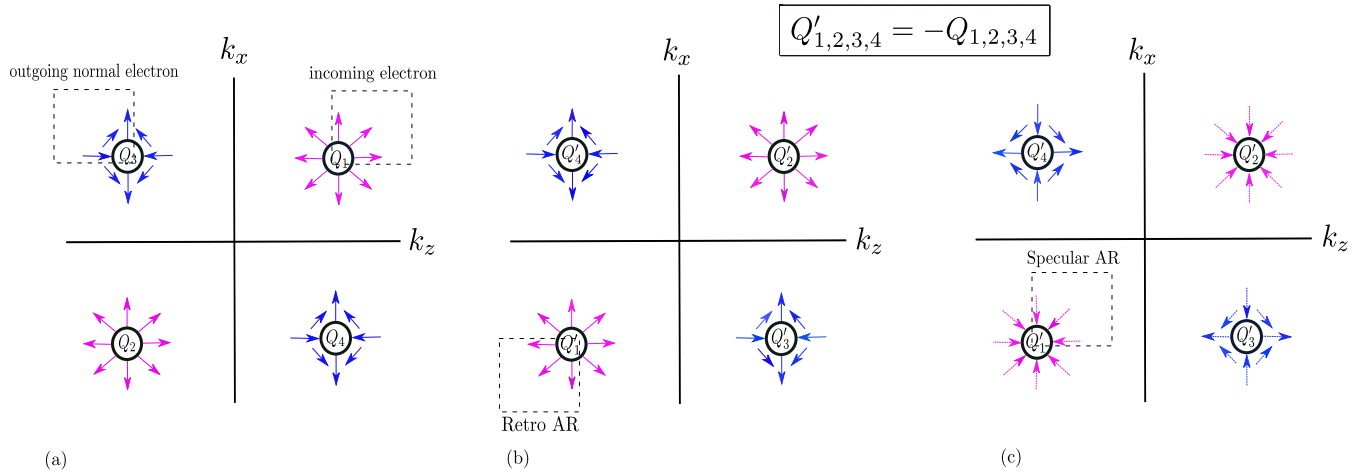
FIG. 3. (a) The spin texture is shown for the lower conduction band near the Weyl cones for an electron. The same is shown for the lower conduction band and lower valence band near the Weyl cones for a hole in panels (b) and (c), respectively. We choose the other model parameters as $\beta = 1$, $k_0 = \sqrt{2}$, and $k_y = 0$.

The wave functions in the WSC region can be written as

$$\Psi_{\overrightarrow{eq}}(z) = (e^{i\beta}\cos\phi_e, e^{i\beta}e^{i\theta_k}\sin\phi_e, e^{-i\alpha}\cos\phi_e, e^{-i\alpha}e^{i\theta_k}\sin\phi_e)^T e^{iq_e z} ,$$

$$\Psi_{\overleftarrow{eq}}(z) = (e^{i\beta}e^{-i\theta_k}\sin\phi_e, e^{i\beta}\cos\phi_e, e^{-i\alpha}e^{-i\theta_k}\sin\phi_e, e^{-i\alpha}\cos\phi_e)^T e^{-iq_e z} ,$$

$$\Psi_{\overrightarrow{hq}}(z) = (e^{i\alpha}e^{-i\theta_k}\cos\phi_h, e^{i\alpha}\sin\phi_h, e^{i\beta}e^{-i\theta_k}\cos\phi_h, e^{i\beta}\sin\phi_h)^T e^{iq_h z} ,$$

$$\Psi_{\overleftarrow{hq}}(z) = (e^{i\alpha}\sin\phi_h, e^{i\alpha}e^{i\theta_k}\cos\phi_h, e^{i\beta}\sin\phi_h, e^{i\beta}e^{i\theta_k}\cos\phi_h)^T e^{-iq_h z} , \tag{10}$$

where $q_{(e,h)} = \sqrt{(\mu_S \pm \Omega)^2 - k_{||}^2}$ and $\phi_{(e,h)} = \tan^{-1}(k_{||}/q_{(e,h)})/2$ are the momenta (close to Weyl points) and incident angles of the electron- and holelike quasiparticles, respectively, inside the superconducting region. For $E \leqslant \Delta$ (subgapped regime), $\beta = \cos^{-1}(E/\Delta)$ and $\Omega = i\sqrt{\Delta^2 - E^2}$, while for $E > \Delta$ (above the gap), $\beta = -i\cosh^{-1}(E/\Delta)$ and $\Omega = \sqrt{E^2 - \Delta^2}$. Considering the scattering between the same chirality Weyl nodes, we can write the scattering states on both sides of the junction as

$$\Psi_<(z) = \psi_{\overrightarrow{e}}(z) + r_e\,\psi_{\overleftarrow{e}}(z) + r_h\,\psi_{\overleftarrow{h}}(z) ,$$

$$\Psi_>(z) = t_e\,\Psi_{\overrightarrow{eq}}(z) + t_h\,\Psi_{\overleftarrow{hq}} , \tag{11}$$

where $r_{e,h}$ corresponds to the normal and AR scattering coefficients, respectively, while $t_{e,h}$ denotes the transmission coefficients for the electron- and holelike quasiparticles, respectively. We obtain the 4×4 scattering matrix by matching the wave functions [Eq. (11)] on both sides of the junction at $z = 0$ ($\Psi_<(z) = \Psi_>(z)|_{z=0}$).

III. THERMAL TRANSPORT

For the noninteracting electrons, the total transmission function for the transport of the electronic charge through the junction can be computed using the scattering matrix approach. Integrating over the transverse modes one can write [28,29]

$$\mathcal{T}(E) = \int \frac{d^2 k_{||}}{4\pi^2} \left(1 - R_e(E) + \mathrm{Re}\left[\frac{\cos 2\varphi_h}{\cos 2\varphi_e}\right] R_h(E)\right), \tag{12}$$

where $k_{||}$ is the momentum parallel to the junction interface, R_e and R_h are the normal and AR probability, respectively, and φ_e and φ_h are the angle of incidence for electron and hole, respectively. Changing the integration variable $k_{||}$ to φ_e using $k_{||} = (E + \mu_N)\sin 2\varphi_e$, we can write

$$\mathcal{T}(E) = \frac{1}{2\pi} \int d\varphi_e \left(1 - R_e(E) + \mathrm{Re}\left[\frac{\cos 2\varphi_h}{\cos 2\varphi_e}\right] R_h(E)\right)$$
$$\times (E + \mu_N)^2 \sin 4\varphi_e . \tag{13}$$

While the electrical charge transport can distinguish between the electron and hole contribution by the sign of R_e and R_h, the thermal transport treats both the electron and the hole as a particle carrying the number density along the same direction (see Appendix A for details). Consequently, for the thermal transport, the transmission function for the energy transport through the junction can be computed using [28,29] as

$$\mathcal{T}_{\text{therm}}(E) = \frac{1}{2\pi} \int d\varphi_e \left(1 - R_e(E) - \mathrm{Re}\left[\frac{\cos 2\varphi_h}{\cos 2\varphi_e}\right] R_h(E)\right)$$
$$\times (E + \mu_N)^2 \sin 4\varphi_e . \tag{14}$$

A. Electrical conductance and thermoelectric coefficient

We begin with the general expression for total electrical current through the normal-superconductor (NS) junction in the presence of voltage and temperature biases [49] as

$$I = \frac{2e}{h} \int_{-\infty}^{\infty} [f_N(E - e\Delta V, T + \Delta T) - f_S(E, T)]\mathcal{T}(E)\, dE \,.$$
(15)

where f_N and f_S are the Fermi distribution functions of the two reservoirs to which the NS setup is attached.

In the linear response regime, one can expand the Fermi functions for very small voltage and temperature differences as

$$f_N(E - e\Delta V, T + \Delta T) = f_0(E, T) - e\Delta V \frac{\partial f_0}{\partial E} + \Delta T \frac{\partial f_0}{\partial T} \,,$$
$$f_S(E, T) = f_0(E, T) \,,$$
(16)

where f_0 is the average Fermi distribution at energy E and temperature T. Using Eq. (16), we can write the total current as (see Appendix A for the complete derivation following Ref. [49])

$$I = \frac{2e}{h} \int_{-\infty}^{\infty} \left[-e\Delta V \frac{\partial f_0}{\partial E} + \Delta T \frac{\partial f_0}{\partial T} \right] \mathcal{T}(E)\, dE \,.$$
(17)

Hence, comparing the total current with the Onsager relation,

$$I = G\Delta V + L_{12}\Delta T \,,$$
(18)

we arrive at the expressions for electrical conductance and the thermoelectric coefficient [50,51] as

$$G = \frac{2e^2}{h} \int_{-\infty}^{\infty} \left(-\frac{\partial f_0}{\partial E} \right) \mathcal{T}(E)\, dE \,,$$

$$L_{12} = -\frac{2e}{h} \int_{-\infty}^{\infty} \left(-\frac{\partial f_0}{\partial T} \right) \mathcal{T}(E)\, dE \,.$$
(19)

B. Thermal conductance, thermopower, and figure of merit

The normalized thermal conductance through the NS interface can be defined as [50]

$$\kappa/\kappa_0 = \int_{-\infty}^{\infty} (E - \mu_N) \left(-\frac{\partial f_0}{\partial T} \right) \mathcal{T}_{\text{therm}}(E)\, dE \,,$$
(20)

where κ_0 is the thermal conductance due to ballistic channels in the bulk at energy $(E + \mu_N)$ and $T = T_c$. This is given by

$$\kappa_0 = \int_{-\infty}^{\infty} dE \frac{(E + \mu_N)^2}{4\pi} (E - \mu_N) \left(\frac{\partial f_0}{\partial T} \right)_{T=T_c} \,.$$
(21)

When a temperature gradient is maintained in a metal and no electric current is allowed to flow, a steady-state electrostatic potential difference builds up between the high- and low-temperature regions. This is called the thermoelectric effect and is measured by the thermopower (the Seebeck coefficient), which by definition is given by [52]

$$S = -\left(\frac{\Delta V}{\Delta T} \right)_{I=0} \,.$$
(22)

Using Eq. (18), the analytical expression for the thermopower can be written as

$$S = \frac{L_{12}}{G} \,,$$
(23)

where S is measured in units of k_B/e.

The performance of a thermoelectric device is characterized by a dimensionless quantity called the figure of merit,

$$zT = \frac{S^2 GT}{\kappa} \,.$$
(24)

The major objective is to attain higher values of figure of merit in different materials/hybrid junctions, which would be desirable for their potential applicability in thermoelectric devices. It is clear from Eq. (24) that this can be achieved by improving electrical transport properties and reducing thermal conductivity.

C. Wiedemann-Franz law

The Wiedemann-Franz (WF) law states that the ratio of thermal conductance κ to electrical conductance G is proportional to the absolute temperature,

$$\frac{\kappa}{G} = \mathcal{L} T \,,$$
(25)

where the proportionality constant $\mathcal{L}$ is a universal number called the Lorentz number. For an ideal Fermi gas, we have $\mathcal{L} = \mathcal{L}_0 = \frac{\pi^2}{3}(\frac{k_B}{e})^2$. Violation of the WF law has been reported for semiconductors [53], zero-gap systems, e.g., graphene [31,54], quasi-one-dimensional Luttinger liquids [55], and heavy-fermion materials [56]. We explore the validity of the WF law in our WSM-WSC setup and unveil several interesting features near the Weyl point, which we discuss in the next section.

IV. NUMERICAL RESULTS

In this section we proceed to discuss our numerical results for thermal transport through the WSM-WSC setup. We compute the scattering probabilities employing Eq. (11) and find the relevant physical quantities using the analytical expressions discussed in Sec. III.

A. Thermal conductance

We compute the normalized thermal conductance using Eq. (20) and show its behavior as a function of temperature in Fig. 4(a). For $\mu_N < \Delta_0$, the thermal conductance remains vanishingly small for lower temperatures and starts increasing exponentially with the enhancement of temperature. The zero value of thermal conductance at $T = 0$ is due to the perfect AR in the subgapped regime, which blocks the thermal transport. When the temperature is very small ($T \ll T_c$), electrons with energy at least μ_N contribute to the thermal conductance. We show this in Fig. 4(a) for $\mu_N/\Delta_0 = 1$ and $\mu_N/\Delta_0 = 2$. Clearly, the thermal conductance increases as we enhance μ_N, due to the availability of more states. The blockage of thermal transport (at $T = 0$) continues as long as the transport is dominated by the superconducting Cooper pairs. Further, thermal conductance exhibits an exponential rise for $\mu_N \leqslant$
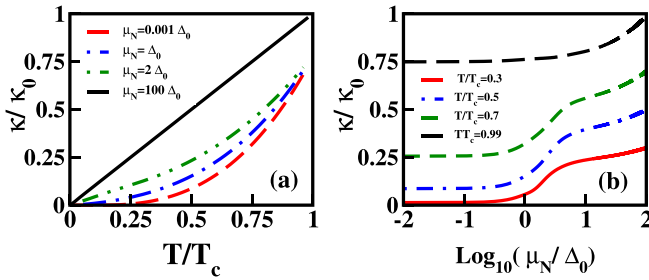
FIG. 4. (a) The behavior of normalized thermal conductance is shown as a function of temperature for $\mu_N/\Delta_0 = 0.001, 1, 2, 100$ represented by dashed, dot-dashed, double dot-dashed, and solid lines, respectively. (b) The normalized thermal conductance with respect to the logarithm of μ_N/Δ_0 is depicted for $T/T_c = 0.3, 0.5, 0.7$ and 0.99, represented by longer dashed, dashed, dot-dashed, and solid lines, respectively.

Δ_0 as one moves towards T_c. We attribute this behavior to the spin-singlet s-wave superconductor in the Weyl NS junction, as has been reported earlier in superconducting hybrid junctions based on Dirac-like materials [23,28,29]. When the chemical potential on the normal WSM side becomes much larger than the superconducting gap, the NS junction becomes transparent and behaves like a metal. The metallic behavior of the thermal conductance is known to be linear with the increase of temperature [57,58], and we find this characteristic for $\mu_N/\Delta_0 = 100$ as shown in Fig. 4(a). This is because at $\mu_N \gg \Delta_0$, the incoming electrons easily overcome the superconducting gap on the right side, which results in a linear increase in thermal conductance.

Further, we discuss the behavior of thermal conductance as a function of chemical potential μ_N in the normal side, at a fixed temperature. To show the clear dependence on μ_N at a larger scale ($0.01\Delta_0$ to $100\Delta_0$), we demonstrate this using log scale for μ_N in Fig. 4(b). It is evident that as we increase the temperature towards T_c, there is a larger enhancement in the thermal conductance as we move away from Δ_0.

B. Wiedemann-Franz law

We discuss the features of the Wiedemann-Franz law in this section. We numerically compute the thermal and electrical conductance to find the Lorentz number (in terms of Lorentz number L_0 for a metal), as given in Eq. (25). We depict the Lorentz number with the variation of the chemical potential in the WSM side of the junction for three values of temperature $T/T_c = 0.99, 0.3, 0.1$ in Fig. 5. The symmetric behavior of the Lorentz number with respect to the chemical potential μ_N is due to the particle-hole symmetry of the system. We generally arrive at the larger Lorentz number when there is a small contribution to the thermal conductance. For moderate temperature (e.g., $T/T_c = 0.3$ in Fig. 5), the Lorentz number is finite, even at $\mu_N = 0$. This is due to the reduction of the superconducting gap with the increase of temperature, and we expect that this is responsible for finite thermal conductance even at $\mu_N < \Delta_0$. Note that there is always a dip in the Lorentz number at the Weyl point ($\mu_N = 0$) below T_c. When $T/T_c = 0.1$, this dip becomes maximum and touches the Weyl point due to the unavailability of density of states.
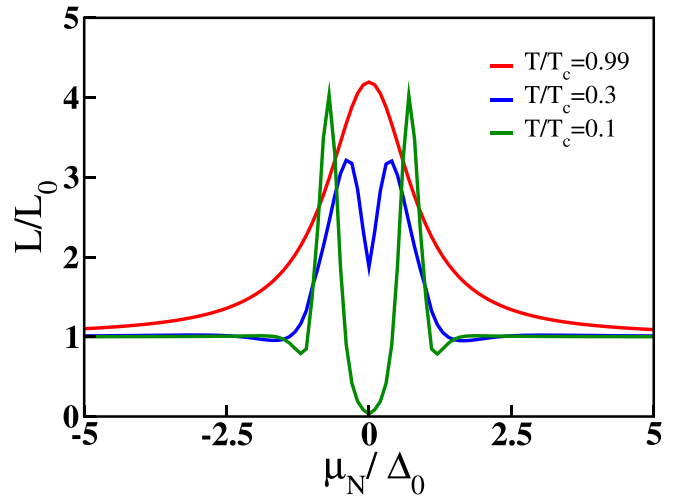
FIG. 5. The variation of Lorentz number, in the WSM-WSC junction, is shown as a function of μ_N for three different values of temperatures. Red, blue, and green color denote the corresponding behavior for $T/T_c = 0.99, 0.3, 0.1$, respectively.

However, at $T/T_c = 0.99$ the superconducting gap becomes vanishingly small, and we find the Lorentz number for the system to be 4.1958 at the Weyl point. This large value can be attributed to the quasiparticle states close to the superconducting gap. We analytically compute the Lorentz number for a bulk WSM (see Appendix B for details) following the semiclassical approach and we find it to be 5.13. This is of the same order of magnitude as the numerical estimate here, where we consider the quantum behavior of the system.

The physical reason behind this peculiar behavior (violation of the WF law) of the Lorentz number within the range $-\Delta_0 < \mu_N < \Delta_0$ can be attributed to the temperature dependence of the superconducting gap in our NS Weyl junction. Such deviations of the WF law from L_0 (close to the Dirac point) have been reported earlier in the case of graphene [31,54]. Beyond this region, the Lorentz number converges to L_0 (Lorentz number for metals) for all temperatures. For $\mu_N > \Delta_0$, the transport occurs via the states above the subgap energy. This means that the WSM-WSC junction becomes transparent to electronic transport, and once again, we witness metal-like behavior as $\mu_N \gg \Delta_0$.

C. Thermopower and figure of merit

Here we analyze the thermopower or Seebeck coefficient that also describes the thermoelectric properties of the system. We have defined this quantity in Sec. III [see Eq. (23)]. We present the observed characteristics of thermopower in Fig. 6 as a function of (a) the doping level μ_N in the WSM side and (b) the temperature T. Note that the thermopower at $T \ll T_c$ can be clearly distinguished from the behavior at $T < T_c$ for all values of μ_N.

The efficiency of converting heat into electricity is related to the thermoelectric figure of merit, zT defined in Sec. III. We compute the dimensionless figure of merit employing $S^2 GT/\kappa$ [Eq. (24)] and show the corresponding behavior in Fig. 7(a) as a function of μ_N/Δ_0 at fixed temperatures. Interestingly, we find larger values of zT for lower temperature ($T \ll T_c$)
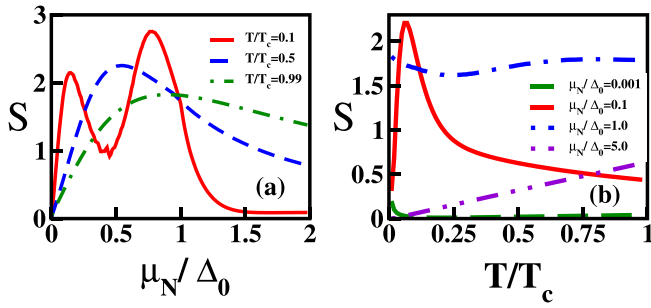
FIG. 6. The behavior of thermopower or Seebeck coefficient (in unit of k_B/e) is depicted as a function of (a) μ_N/Δ_0 for $T/T_c = 0.1, 0.5, 0.99$ represented by red (solid), blue (dash), and green (dot-dash) lines, respectively, and (b) T/T_c for $\mu_N/\Delta_0 = 0.001, 1, 2, 100$ represented by green (dash), red (solid), blue (dot-dash), and purple (double dot-dash) lines, respectively.

and doping ($\mu_N \ll \Delta_0$), as shown in Fig. 7(a). Quantitatively, such high values of zT arise due to small values of κ and large S in this regime. However, we do not fully understand the physical reason behind having such a large value of zT. Nevertheless, we note that the two-dimensional Dirac materials, whose low energy dispersion is effectively described by the massless Dirac Hamiltonian, have been shown to maximize zT up to 15 [59]. The behavior of zT is also shown in Fig. 7(b) as a function of temperature for fixed μ_N. Note that high values of $zT \sim 9$–10 also appear for low temperatures when $\mu_N/\Delta_0 \ll 1$.

D. Effect of insulating barrier

In this section we investigate the changes in thermoelectric properties caused by an insulating barrier introduced at the WSM-WSC interface (see Fig. 2). We assume the barrier to be of length d and height V_0. This can be modeled as $U(z) = V_0 \Theta(z)\Theta(d - z)$. We carry out our analysis by matching the wave function at the two interfaces, assuming one to be at $z = 0$ and the other at $z = d$. The wave function in the insulating region can be written as Eq. (9), with μ_N replaced by $\mu_N - V_0$. Here we consider the thin barrier limit. In this limit
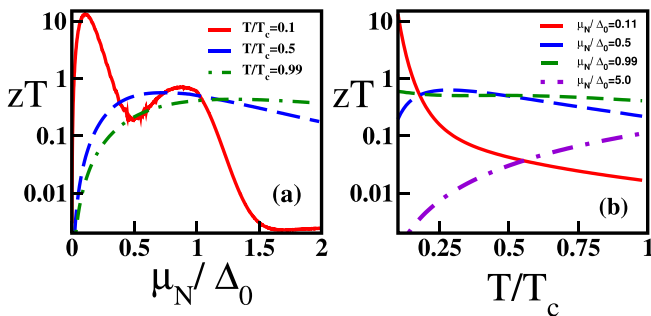
FIG. 7. The figure of merit zT is depicted in the log scale as a function of (a) μ_N/Δ_0 for $T/T_c = 0.1, 0.5, 0.99$ represented by red (solid), blue (dash), and green (dot-dash) lines, respectively, and (b) T/T_c for $\mu_N/\Delta_0 = 0.11, 0.5, 0.99, 5$ denoted by red (solid), blue (large dash), green (small dash), and purple (dot-dash) lines, respectively.

one can define a finite quantity $\chi = V_0 d$ [29] with $V_0 \to \infty$ and $d \to 0$, called the strength of the barrier. We present here the distinctive behavior of the thermoelectric properties with respect to this barrier strength χ.

To begin with we show the behavior of thermal conductance with the variation of χ in Fig. 8(a). Clearly, π-periodic oscillations in κ are found for larger doping ($\mu_N/\Delta_0 = 100$). On the other hand, the amplitude of oscillations becomes negligibly small as one decreases μ_N. We also find that the maximum amplitude (difference between $|\kappa(\chi = 0) - \kappa(\chi = \pi/2)|$) of oscillations increases as we increase the value of μ_N at any fixed temperature. We present this behavior in Fig. 8(b). The maximum amplitude of oscillations increases more rapidly as one approaches $T \to T_c$ for $\mu_N \gg \Delta_0$.

Afterwards, we study thermopower S with the variation of T/T_c for different values of χ and show its corresponding behavior in Fig. 9(a). Note that the thermopower changes sign for $\chi = \pi/3, \pi/2$. This characteristic feature of changing sign in thermopower is also clearly visible in Fig. 9(b), where we illustrate its behavior with respect to χ for different values of $\mu_N \ll \Delta_0$. We expect that this sign change in S takes place due to the electrons close to the Weyl point.

V. SUMMARY AND DISCUSSION

To summarize, in this work we have investigated thermal transport through normal-superconductor junctions of inversion symmetry broken Weyl semimetals (WSM-WSC

FIG. 8. (a) The normalized thermal conductance is depicted as a function of the barrier strength χ at $\mu_N/\Delta_0 = 0.001, 0.1, 1, 100$, $T/T_c = 0.5$. (b) The maximum amplitude of the thermal conductance oscillations as a function of μ_N is shown in the log scale at $T/T_c = 0.99, 0.5, 0.1$.
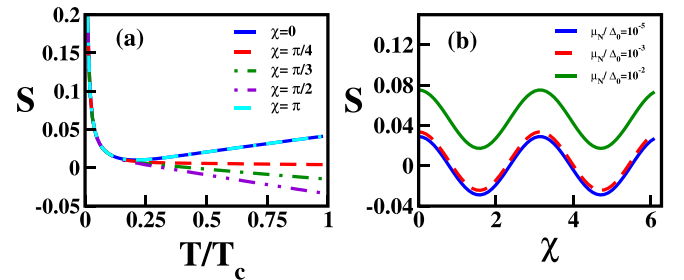
FIG. 9. (a) Thermopower S is shown as a function of temperature at $\chi = 0, \pi/4, \pi/3, \pi/2, \pi$. Here we choose $\mu_N/\Delta_0 = 0.001$. (b) S is depicted with the variation of insulating barrier strength χ at $\mu_N/\Delta_0 = 10^{-5}, 10^{-3}, 10^{-2}$ and $T/T_c = 0.8$.

heterostructures). We have discussed the characteristic features of thermal conductance, thermopower, and figure of merit under different sets of parameter values. We have shown that the normalized thermal conductance has the conventional exponential dependence on the temperature for lower dopings (chemical potential μ_N on the WSM side), while it exhibits the typical linear behavior like in metals for higher doping. We find that the Lorentz number shows interesting features below the superconducting gap. This includes the violation of the Wiedemann-Franz law for $-\Delta_0 < \mu_N < \Delta_0$ and agreement (metal like) for higher doping concentrations ($|\mu_N| \gg \Delta_0$). Further, we have studied the thermopower/Seebeck coefficient and the figure of merit. Surprisingly, the figure of merit shows a sharp increase for transport near the Weyl point, while it stays close to unity away from it. In addition, we have also investigated the effect of a thin insulating barrier on the thermal conductance and thermopower. Importantly, we find larger oscillations (with period π) in the thermal conductance with the variation of barrier strength for larger doping and negligible oscillation amplitudes for smaller doping concentrations. Moreover, very close to the Weyl point, the thermopower is shown to change sign from positive to negative as we increase the barrier strength χ.

As far as a practical realization of our setup is concerned, WSM-WSC heterostructures may be possible to fabricate with appropriate materials, although the material realization of WSC is still not known, to the best of our knowledge. Within our setup, the chemical potentials μ_N and μ_S can be tuned via two additional external gate voltages. These gate voltages can modulate the Fermi energy (doping level) of the normal and superconducting sides of the junction. In particular, one gate voltage can tune μ_N over the entire sample. The other chemical potential, $\mu_S = \mu_N + U_0$, can be independently modulated by tuning U_0 by another gate voltage. For a typical value of $\Delta_0 \sim 1.3$ meV, it may be possible to achieve a high value of $zT \sim 9 - 10$ at low temperatures ($T \sim 1 - 2$ K) and chemical potentials of $\mu_N \sim 0.15$ meV.

APPENDIX A: DERIVATION OF EQ. (17), I.E., THE TOTAL CURRENT

We follow Ref. [49] to arrive at Eq. (17) (see in main text) for one-dimensional transport. This derivation is potentially important for understanding thermoelectric coefficients L_{12}. This physical quantity plays a significant role in determining the thermoelectric properties of any device, namely, thermopower or Seebeck coefficient. Thermoelectric current (determined by the thermoelectric coefficient) is conceptually a net charge transfer due to temperature bias. We schematically show the normal-superconductor (NS) junction in Fig. 10, where we assume that the left and right reservoirs are kept at bias voltages $E - e\Delta V$ and E, respectively, as
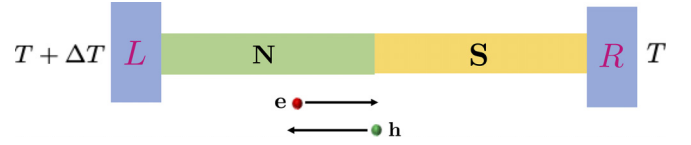
FIG. 10. Cartoon of a NS junction that is attached to left (L) and right (R) reservoirs which are kept at temperatures $T + \Delta T$ and T, respectively. The red and green dots represent the flow of electrons and holes, respectively, due to the applied thermal bias.

well as at temperatures $T + \Delta T$ and T, respectively. The flow of electrons from the higher to the lower temperature region would cause a flow of electric current from left to right, as depicted by the electron flow indicated by a red dot in Fig. 10. The flow direction of the Andreev-reflected hole is denoted by a green dot.

The total current through the NS junction can be read from Ref. [49] as

$$I = \frac{2e}{h} \int_{-\infty}^{\infty} [f_\rightarrow(E) - f_\leftarrow(E)]dE \ , \tag{A1}$$

where, $f_\rightarrow(E)$ and $f_\leftarrow(E)$ are the distribution functions of particles coming from N and S side of the junction, respectively.

The distribution functions for finite voltage and temperature bias are given by

$$
\begin{aligned}
f_\rightarrow(E) &= f_0(E - e\Delta V, T + \Delta T), \\
f_\leftarrow(E) &= A(E)[1 - f_\rightarrow(-E, T - \Delta T)] \\
&\quad + B(E)f_\rightarrow(E, T + \Delta T) \\
&\quad + [C(E) + D(E)]f_0(E, T) \\
&= A(E)f_0(E + e\Delta V, T - \Delta T) \\
&\quad + B(E)f_0(E - e\Delta V, T + \Delta T) \\
&\quad + [1 - A(E) - B(E)]f_0(E, T) \ , \tag{A2}
\end{aligned}
$$

where we use $1 - f_\rightarrow(-E, T - \Delta T) = f_0(E + e\Delta V, T - \Delta T)$ and $A(E) + B(E) + C(E) + D(E) = 1$ to arrive at the last expression. We then Taylor expand the distribution functions for small voltage and temperature biases (linear response regime) as

$$
\begin{aligned}
f_0(E - e\Delta V, T + \Delta T) &= f_0(E, T) - e\Delta V \frac{\partial f_0}{\partial E} + \Delta T \frac{\partial f_0}{\partial T}, \\
f_0(E + e\Delta V, T - \Delta T) &= f_0(E, T) + e\Delta V \frac{\partial f_0}{\partial E} - \Delta T \frac{\partial f_0}{\partial T}.
\end{aligned} \tag{A3}
$$

Using Eq. (A3), we arrive at the current expression for one-dimensional transport as

$$I = \frac{2e}{h} \int_{-\infty}^{\infty} \left[-e\Delta V \frac{\partial f_0}{\partial E} + \Delta T \frac{\partial f_0}{\partial T} \right](1 + A - B)\, dE \ .$$

Therefore, from the Onsager relation [see Eq. (18)] one can arrive at the expression for L_{12} as [50]

$$L_{12} = -\frac{2e}{h} \int_{-\infty}^{\infty} \left(-\frac{\partial f_0}{\partial T} \right)[1 + A(E) - B(E)]\, dE \ . \tag{A4}$$

APPENDIX B: WIEDEMANN-FRANZ LAW FOR BULK WEYL SEMIMETAL CLOSE TO THE WEYL POINT

In this Appendix we provide an analytical derivation of the WF law for the three-dimensional (3D) bulk WSM near the Weyl point. The idea is to compare this with the Lorentz number for a WSM-WSC junction close to critical temperature ($T \sim T_c$) and $\mu_N \sim 0$, which is discussed in the main text and shown in Fig. 5. We note that following the Blonder-Tinkham-Klapwijk approach [49], we numerically find the Lorentz number to be 4.1958 for $\mu_N = 0$. Here we follow a semiclassical approach, which is adopted in a recent study of WF law in the case of bulk graphene [60].

The general expression of thermal conductivity κ relating to the specific heat C of the system is given by

$$\kappa = \frac{1}{d} C v_F \langle l \rangle , \tag{B1}$$

where d, v_F, and $\langle l \rangle$ are the dimension, Fermi velocity, and average mean free path, respectively, for the corresponding system.

We compute the specific heat and the mean free path of a bulk 3D WSM considering the low-energy effective linear spectrum $\epsilon_p = \hbar v_F |p|$. Using the density of states close to the Weyl point as $D(E) = E^2/2\pi^2(\hbar v_F)^3$, the specific heat of the system in terms of the internal energy is

$$C = \frac{dU}{dT} = \frac{d}{dT}\left[\int_0^\infty dE \, D(E) \, f(E) \, E \right] , \tag{B2}$$

where $f(E)$ is the Fermi distribution function. After a few steps of algebra we arrive at the expression for C in a WSM given by

$$C = \frac{4}{\pi^2} \frac{k_B^4 T^3}{(\hbar v_F)^3} (5.6822) . \tag{B3}$$

To calculate the mean free path, we use the Drude formula which relates the electrical conductivity to the mean free path of electrons in the system as

$$G = \frac{n e^2 l}{m^* v_F} , \tag{B4}$$

where m^* and n denote the effective mass and number density of electrons, respectively.

Using the number density $n = k_F^3/6\pi^2$ and considering only the transport along the z direction, we find the mean free path as

$$l = G \frac{6 \pi^2 \hbar^3 v_F^2}{E^2 e^2} . \tag{B5}$$

Here the effective mass of the system in general is defined as

$$m_{ij}^* = \frac{\hbar^2}{\left(\frac{\partial^2 E}{\partial p_i \partial p_j} \right)} . \tag{B6}$$

For a spherical Fermi surface, off-diagonal components of the effective mass tensor become zero. Therefore the remaining terms are $m_{xx}^* = m_{yy}^* = m_{zz}^* = \frac{\hbar p_F}{v_F}$. For transport along z direction, we have $m_{zz}^* = m^* = \frac{\hbar p_F}{v_F}$.

Hence the average mean free path can be found as

$$\langle l \rangle = G \frac{6 \pi^2 \hbar^3 v_F^2}{e^2} \left\langle \frac{1}{E^2} \right\rangle . \tag{B7}$$

Computing the average value of $1/E^2$ statistically, we find the analytical expression of average mean free path as

$$\langle l \rangle = G \frac{6 \pi^2 \hbar^3 v_F^2}{e^2} \left\langle \frac{0.384423}{(k_B T^2)} \right\rangle . \tag{B8}$$

Using the specific heat in Eq. (B3) and the average mean free path in Eq. (B8), one can compute the thermal conductance employing Eq. (B1). Finally, substituting this quantity in Eq. (25), we arrive at the Lorentz number,

$$L = \frac{\kappa}{G T} = 5.3171 \times L_0 , \tag{B9}$$

where $L_0 = \frac{\pi^2}{3}\left(\frac{k_B}{e}\right)^2$.

[1] S. L. Adler, Axial-vector vertex in spinor electrodynamics, Phys. Rev. **177**, 2426 (1969).

[2] J. S. Bell and R. A Jackiw, A PCAC puzzle: $\pi^0 \to \gamma\gamma$ in the σ model, Nuovo Cimento A (1965-1970) **60**, 47 (1969).

[3] K. Fukushima, D. E. Kharzeev, and H. J. Warringa, Chiral magnetic effect, Phys. Rev. D **78**, 074033 (2008).

[4] N. P. Armitage, E. J. Mele, and A. Vishwanath, Weyl and Dirac semimetals in three-dimensional solids, Rev. Mod. Phys. **90**, 015001 (2018).

[5] S.-M. Huang, S.-Y. Xu, I. Belopolski, C.-C. Lee, G. Chang, B. Wang, N. Alidoust, G. Bian, M. Neupane, C. Zhang, S. Jia, A. Bansil, H. Lin, and M. Z. Hasan, A Weyl Fermion semimetal with surface Fermi arcs in the transition metal monopnictide TaAs class, Nat. Commun. **6**, 7373 (2015).

[6] S. Y. Xu, I. Belopolski, D. S. Sanchez, C. L. Zhang, G. Q. Chang, C. Guo, G. Bian, Z. J. Yuan, H. Lu, T. R. Chang, P. P. Shibayev, M. L. Prokopovych, N. Alidoust, H. Zheng, C. C. Lee, S. M. Huang, R. Sankar, F. C. Chou, C. H. Hsu, H. T. Jeng, A. Bansil, T. Neupert, V. N. Strocov, H. Lin, S. Jia, and M. Z. Hasan, Experimental discovery of a topological Weyl semimetal state in TaP, Sci. Adv. **1**, e1501092 (2015).

[7] M. M. Vazifeh and M. Franz, Electromagnetic Response of Weyl Semimetals, Phys. Rev. Lett. **111**, 027201 (2013).

[8] A. A. Zyuzin and A. A. Burkov, Topological response in Weyl semimetals and the chiral anomaly, Phys. Rev. B **86**, 115133 (2012).

[9] B. Q. Lv, H. M. Weng, B. B. Fu, X. P. Wang, H. Miao, J. Ma, P. Richard, X. C. Huang, L. X. Zhao, G. F. Chen, Z. Fang, X. Dai, T. Qian, and H. Ding, Experimental Discovery of Weyl Semimetal TaAs, Phys. Rev. X **5**, 031013 (2015).

[10] A. A. Burkov, M. D. Hook, and L. Balents, Topological nodal semimetals, Phys. Rev. B **84**, 235126 (2011).

[11] B. Yan and C. Felser, Topological materials: Weyl semimetals, Annu. Rev. Condens. Matter Phys. **8**, 337 (2017).

[12] Y. Zhou, Y.-Q. Zhao, Z.-Y. Zeng, X.-R. Chen, and H.-Y. Geng, Anisotropic thermoelectric properties of Weyl semimetal NbX (X = P and As): A potential thermoelectric material, Phys. Chem. Chem. Phys. **21**, 15167 (2019).

[13] D. Chang, Y. Liu, F. Rao, F. Wang, Q. Sunac, and Y. Jia, Phonon and thermal expansion properties in Weyl semimetals MX (M = Nb, Ta; X = P, As): Ab initio studies, Phys. Chem. Phys. **18**, 14503 (2016).

[14] Y. Sun, S.-C. Wu, and B. Yan, Topological surface states and fermi arcs of the noncentrosymmetric Weyl semimetals TaAs, TaP, NbAs, and NbP, Phys. Rev. B **92**, 115428 (2015).

[15] B. Q. Lv, N. Xu, H. M. Weng, J. Z. Ma, P. Richard, X. C. Huang, L. X. Zhao, G. F. Chen, C. E. Matt, F. Bisti, V. N. Strocov, J. Mesot, Z. Fang, X. Dai, T. Qian, M. Shi, and H. Ding, Observation of Weyl nodes in TaAs, Nat. Phys. **11**, 724 (2015).

[16] L. X. Yang, Z. K. Liu, Y. Sun, H. Peng, H. F. Yang, T. Zhang, B. Zhou, Y. Zhang, Y. F. Guo, M. Rahn, D. Prabhakaran, Z. Hussain, S. K. Mo, C. Felser, B. Yan, and Y. L. Chen, Weyl semimetal phase in the non-centrosymmetric compound TaAs, Nat. Phys. **11**, 728 (2015).

[17] V. Chandrasekhar, Thermal transport in superconductor/normal-metal structures, Supercond. Sci. Technol. **22**, 083001 (2009).

[18] P. Machon, M. Eschrig, and W. Belzig, Giant thermoelectric effects in a proximity-coupled superconductor–ferromagnet device, New J. Phys. **16**, 073002 (2014).

[19] A. Ozaeta, P. Virtanen, F. S. Bergeret, and T. T. Heikkilä, Predicted Very Large Thermoelectric Effect in Ferromagnet-Superconductor Junctions in the Presence of a Spin-Splitting Magnetic Field, Phys. Rev. Lett. **112**, 057001 (2014).

[20] M. S. Kalenkov, A. D. Zaikin, and L. S. Kuzmin, Theory of a Large Thermoelectric Effect in Superconductors Doped with Magnetic Impurities, Phys. Rev. Lett. **109**, 147004 (2012).

[21] P. Machon, M. Eschrig, and W. Belzig, Nonlocal Thermoelectric Effects and Nonlocal Onsager relations in a Three-Terminal Proximity-Coupled Superconductor-Ferromagnet Device, Phys. Rev. Lett. **110**, 047002 (2013).

[22] S. Kolenda, M. J. Wolf, and D. Beckmann, Observation of Thermoelectric Currents in High-Field Superconductor-Ferromagnet Tunnel Junctions, Phys. Rev. Lett. **116**, 097001 (2016).

[23] P. Dutta, A. Saha, and A. M. Jayannavar, Thermoelectric properties of a ferromagnet-superconductor hybrid junction: Role of interfacial Rashba spin-orbit interaction, Phys. Rev. B **96**, 115404 (2017).

[24] M. M. Wysokinski and J. Spalek, Seebeck effect in the graphene-superconductor junction, J. Appl. Phys. **113**, 163905 (2013).

[25] M. Zebarjadi, K. Esfarjani, M. S. Dresselhaus, Z. F. Ren, and G. Chen, Perspectives on thermoelectrics: From fundamentals to device applications, Energy Environ. Sci. **5**, 5147 (2012).

[26] G. J. Snyder and E. S. Toberer, Complex thermoelectric materials, Nat. Mater. **7**, 105 (2008).

[27] F. Giazotto, T. T. Heikkilä, A. Luukanen, A. M. Savin, and J. P. Pekola, Opportunities for mesoscopics in thermometry and refrigeration: Physics and applications, Rev. Mod. Phys. **78**, 217 (2006).

[28] T. Yokoyama, J. Linder, and A. Sudbø, Heat transport by Dirac fermions in normal/superconducting graphene junctions, Phys. Rev. B **77**, 132503 (2008).

[29] G. C. Paul, S. Sarkar, and A. Saha, Thermal conductance by Dirac fermions in a normal-insulator-superconductor junction of silicene, Phys. Rev. B **94**, 155453 (2016).

[30] R. Beiranvand and H. Hamzehpour, Spin-dependent thermoelectric effects in graphene-based superconductor junctions, J. Appl. Phys. **121**, 063903 (2017).

[31] T. Y. Kim, C.-H. Park, and N. Marzari, The electronic thermal conductivity of graphene, Nano Lett. **16**, 2439 (2016).

[32] H. Sevinçli and G. Cuniberti, Enhanced thermoelectric figure of merit in edge-disordered zigzag graphene nanoribbons, Phys. Rev. B **81**, 113401 (2010).

[33] M. Zare, Negative differential thermal conductance in a borophane normal metal–superconductor junction, Supercond. Sci. Technol. **32**, 115002 (2019).

[34] S. Uchida, T. Habe, and Y. Asano, Andreev reflection in Weyl semimetals, J. Phys. Soc. Jpn. **83**, 064711 (2014).

[35] U. Khanna, D. K. Mukherjee, A. Kundu, and S. Rao, Chiral nodes and oscillations in the Josephson current in Weyl semimetals, Phys. Rev. B **93**, 121409(R) (2016).

[36] D. K. Mukherjee, S. Rao, and A. Kundu, Transport through Andreev bound states in a Weyl semimetal quantum dot, Phys. Rev. B **96**, 161408(R) (2017).

[37] S.-B. Zhang, F. Dolcini, D. Breunig, and B. Trauzettel, Appearance of the universal value e^2/h of the zero-bias conductance in a Weyl semimetal-superconductor junction, Phys. Rev. B **97**, 041116(R) (2018).

[38] Y. Zheng, W. Chen, and D. Y. Xing, Andreev reflection in Fermi-arc surface states of Weyl semimetals, Phys. Rev. B **104**, 075420 (2021).

[39] P. Dutta, F. Parhizgar, and A. M. Black-Schaffer, Finite bulk Josephson currents and chirality blockade removal from interorbital pairing in magnetic Weyl semimetals, Phys. Rev. B **101**, 064514 (2020).

[40] U. Stockert, R. D. dos Reis, M. O. Ajeesh, S. J. Watzman, M. Schmidt, C. Shekhar, J. P. Heremans, C. Felser, M. Baenitz, and M. Nicklas, Thermopower and thermal conductivity in the Weyl semimetal NbP, J. Phys.: Condens. Matter **29**, 325701 (2017).

[41] Q. Chen and G. A. Fiete, Thermoelectric transport in double-Weyl semimetals, Phys. Rev. B **93**, 155125 (2016).

[42] R. Lundgren, P. Laurell, and G. A. Fiete, Thermoelectric properties of Weyl and Dirac semimetals, Phys. Rev. B **90**, 165115 (2014).

[43] T. Meng and L. Balents, Weyl superconductors, Phys. Rev. B **86**, 054504 (2012).

[44] G. Y. Cho, J. H. Bardarson, Y.-M. Lu, and J. E. Moore, Superconductivity of doped Weyl semimetals: Finite-momentum pairing and electronic analog of the ^{3}He $-a$ phase, Phys. Rev. B **86**, 214514 (2012).

[45] G. Bednik, A. A. Zyuzin, and A. A. Burkov, Superconductivity in Weyl metals, Phys. Rev. B **92**, 035153 (2015).

[46] N. Bovenzi, M. Breitkreiz, P. Baireuther, T. E. O'Brien, J. Tworzydło, İ. Adagideli, and C. W. J. Beenakker, Chirality blockade of Andreev reflection in a magnetic Weyl semimetal, Phys. Rev. B **96**, 035437 (2017).

[47] S.-B. Zhang, J. Erdmenger, and B. Trauzettel, Chirality Josephson Current Due to a Novel Quantum Anomaly in

Inversion-Asymmetric Weyl Semimetals, Phys. Rev. Lett. **121**, 226604 (2018).

[48] C. W. J. Beenakker, Specular Andreev Reflection in Graphene, Phys. Rev. Lett. **97**, 067007 (2006).

[49] G. E. Blonder, M. Tinkham, and T. M. Klapwijk, Transition from metallic to tunneling regimes in superconducting microconstrictions: Excess current, charge imbalance, and supercurrent conversion, Phys. Rev. B **25**, 4515 (1982).

[50] R. A. Riedel and P. F. Bagwell, Current-voltage relation of a normal-metal–superconductor junction, Phys. Rev. B **48**, 15198 (1993).

[51] U. Sivan and Y. Imry, Multichannel Landauer formula for thermoelectric transport with application to thermopower near the mobility edge, Phys. Rev. B **33**, 551 (1986).

[52] N. W. Ashcroftand and N. D. Mermin, *Solid State Physics* (Harcourt Asia Pte. Ltd., Singapore, 1976).

[53] H. J. Goldsmid, The thermal conductivity of bismuth telluride, Proc. Phys. Soc. B **69**, 203 (1956).

[54] J. Crossno, J. K. Shi, K. Wang, X. Liu, A. Harzheim, A. Lucas, S. Sachdev, P. Kim, T. Taniguchi, K. Watanabe, T. A. Ohki, and K. C. Fong, Observation of the Dirac fluid and the breakdown of the Wiedemann-Franz law in graphene, Science **351**, 1058 (2016).

[55] N. Wakeham, A. Bangura, X. Xu, J. F. Mercure, M. Greenblatt, and N. E. Hussey, Gross violation of the Wiedemann-Franz law in a quasi one dimensional conductor, Nat. Commun. **2**, 396 (2011).

[56] M. A. Tanatar, J. Paglione, C. Petrovic, and L. Taillefer, Anisotropic violation of the Wiedemann-Franz law at a quantum critical point, Science **316**, 1320 (2007).

[57] B. C. Gundrum, D. G. Cahill, and R. S. Averback, Thermal conductance of metal-metal interfaces, Phys. Rev. B **72**, 245426 (2005).

[58] R. Ghanbari and G. Rashedi, The Wiedemann-Franz law in a normal metal-superconductor junction, Chin. Phys. B **20**, 127401 (2011).

[59] E. H. Hesdeo, L. P. A. Krisna, M. Y. Hanna, B. E. Gunara, N. T. Hung, and A. R. T. Nugraha, Optimal band gap for improved thermoelectric performance of two-dimensional materials, J. Appl. Phys. **126**, 035109 (2019).

[60] A. Rycerz, Wiedemann–Franz law for massless Dirac fermions with implications for graphene, Materials **14**, 2704 (2021).